

A Wide Orbit Exoplanet OGLE-2012-BLG-0838Lb

R. POLESKI,^{1,2} B. S. GAUDI,¹ XIAOJIA XIE,³ A. UDALSKI,² AND J. C. YEE⁴

J. SKOWRON,⁵ M. K. SZYMAŃSKI,⁵ I. SOSZYŃSKI,⁵ P. PIETRUKOWICZ,⁵ S. KOZŁOWSKI,⁵
L. WYRZYKOWSKI,⁵ K. ULACZYK,^{5,6} C. HAN,⁷ SUBO DONG,³ K. M. MORZINSKI,⁸ J. R. MALES,⁸
L. M. CLOSE,⁸ A. GOULD,^{9,10,11} R. W. POGGE,¹¹ J.-P. BEAULIEU,^{12,13} AND J.-B. MARQUETTE^{14,13}

¹*Department of Astronomy, Ohio State University, 140 W. 18th Ave., Columbus, OH 43210, USA*

²*Warsaw University Observatory, Al. Ujazdowskie 4, 00-478 Warszawa, Poland*

³*Kavli Institute for Astronomy and Astrophysics, Peking University, Yi He Yuan Road 5, Hai Dian District, Beijing 100871, China*

⁴*Harvard-Smithsonian Center for Astrophysics, 60 Garden Street, Cambridge, MA 02138, USA*

⁵*Warsaw University Observatory, Al. Ujazdowskie 4, 00-478 Warszawa, Poland*

⁶*Department of Physics, University of Warwick, Coventry CV4 7AL, UK*

⁷*Department of Physics, Chungbuk National University, Cheongju 28644, Republic of Korea*

⁸*Steward Observatory, University of Arizona, Tucson, AZ 85721, USA*

⁹*Max-Planck-Institute for Astronomy, Königstuhl 17, 69117 Heidelberg, Germany*

¹⁰*Korea Astronomy and Space Science Institute, 776 Daedukdae-ro, Yuseong-gu, Daejeon 34055, Korea*

¹¹*Department of Astronomy, Ohio State University, 140 W. 18th Ave., Columbus, OH 43210, USA*

¹²*School of Natural Sciences, University of Tasmania, Private Bag 37 Hobart, Tasmania 7001 Australia*

¹³*Sorbonne Universités, UPMC Université Paris 6 et CNRS, UMR 7095, Institut d'Astrophysique de Paris, 98 bis bd Arago, F-75014 Paris, France*

¹⁴*Laboratoire d'Astrophysique de Bordeaux, Univ. Bordeaux, CNRS, B18N, alle Geoffroy Saint-Hilaire, F-33615 Pessac, France*

(Received ABCDEF XX, 2018; Revised ABCDEF XX, 2018; Accepted January 18, 2019)

Submitted to ApJ

ABSTRACT

We present the discovery of a planet on a very wide orbit in the microlensing event OGLE-2012-BLG-0838. The signal of the planet is well separated from the main peak of the event and the planet-star projected separation is found to be twice larger than the Einstein ring radius, which roughly corresponds to a projected separation of ≈ 4 AU. Similar planets around low-mass stars are very hard to find using any technique other than microlensing. We discuss microlensing model fitting in detail and discuss the prospects for measuring the mass and distance of lens system directly.

Keywords: gravitational lensing: micro — planets and satellites: detection

1. INTRODUCTION

The exoplanets known today show a large degree of diversity. For example, we now know: a planetary system orbiting a pulsar (PSR1257+12; [Wolszczan & Frail 1992](#)), extremely short period planets (55 Cnc e; [Winn et al. 2011](#)), planets with extremely high surface temperatures (KELT-9b; [Gaudi et al. 2017](#)), rocky planets in the habitable zone (Kepler-186f; [Quintana et al. 2014](#)), a gas giant planet orbiting a brown dwarf (2M1207b; [Chauvin et al. 2004](#)), and an Earth-mass planet around an ultracool dwarf (OGLE-2016-BLG-1195; [Shvartzvald et al. 2017](#)), to name a few. These planets have been discovered using a few different detection techniques, and each technique has distinct capabilities and limitations. By far the largest number of planets were discovered using the transit technique, and in particular the *Kepler* satellite yield was very high ([Coughlin et al. 2016](#)). *Kepler* exoplanets are on orbits similar to the inner planets in the Solar System or more compact than that of Mercury. The longest period confirmed transiting exoplanets are: Kepler-1647b (1108 days; [Kostov et al. 2016](#)), Kepler-167e (1071 days; [Kipping et al. 2016](#)), and Kepler-1654b (1048 days; [Beichman et al. 2018](#)). The orbital periods of these planets are shorter than the orbital periods of all Solar System gas and ice giants. The lack of a large number of the long-period planets hampers our understanding of the formation of planetary systems as a whole and Solar System in particular.

Different planet detection techniques have different limitations when it comes to the wide orbit planets. The radial velocity (RV) technique is intrinsically limited by the length of the time-baseline of the RV surveys ([Kane 2011](#); [Sahlmann et al. 2016](#); [Wittenmyer et al. 2017](#)). The limit set by the long-term stability of the spectrographs makes detection of the Neptune-mass planets much more difficult than the Jupiter-mass planets: the RV signals are 0.5 m s^{-1} and 9 m s^{-1} , respectively, for a Neptune-mass and a Jupiter-mass planet on a 10 AU edge-on orbit around $1 M_{\odot}$ star. Astrometric detection of planets on relatively wide orbits can be done using *Gaia* data (in particular, if the mission is significantly extended) or by combining *Gaia* and *Hipparcos* data ([Perryman et al. 2014](#); [Snellen & Brown 2018](#)). The astrometric technique is also sensitive down to Jupiter-mass objects. Direct imaging discovers self-luminous planets that orbit nearby young stars and allows follow-up studies of detected objects ([Bowler 2016](#)). Existing instruments are not sensitive enough to detect planets with masses similar to Neptune. Finally, the microlensing technique finds planets that are a few kiloparsecs (kpc) away and mostly around low-mass (hence mostly old) stars. The on-going microlensing surveys are sensitive to planet/star mass ratios smaller than 10^{-3} even for wide orbit planets. In fact the widest orbit microlensing planet has mass ratio of 2.4×10^{-4} (OGLE-2008-BLG-092LAb; [Poleski et al. 2014](#)). Even for planets that have no detectable stellar host and are likely free-floating, microlensing can probe Neptune-mass planets ([Mróz et al. 2018](#)).

It is important to combine the constraints of both the wide-orbit and the free-floating planets ([Mróz et al. 2017](#)) in order to fully understand the formation and evolution of planetary systems. The bound planet parameters that are readily measured for microlensing are the mass ratio (q) and the projected separation (s) in units of the Einstein ring radius (θ_E). The microlensing planets with the widest orbits are OGLE-2008-BLG-092LAb ($s = 5.3$; [Poleski et al. 2014](#)), OGLE-2011-BLG-0173Lb ($s = 4.6$; [Poleski et al. 2018](#)), and KMT-2016-BLG-1107Lb ($s = 3.0$; [Hwang et al. 2019](#)) – see discussion in [Poleski et al. \(2018\)](#). There are only a few more planets with $s > 2$. For a typical configuration, θ_E corresponds to around 2.5 AU. Hence, the three widest-orbit planets are at projected separations from 7 to 15 AU. The distribution of microlensing planets as a whole has already been studied statistically (e.g., [Gould et al. 2010](#); [Cassan et al. 2012](#); [Suzuki et al. 2016](#); [Udalski et al. 2018](#)), but

the statical properties of the wide-orbit planets have not yet been comprehensively analyzed, partly due to the small number of known wide-orbit planets.

Here we present the discovery of a wide-orbit exoplanet OGLE-2012-BLG-0838Lb. A short-lasting anomaly is observed well before the main peak of the event and this points to an $s = 2.1$ planet. The wide-orbit planet interpretation is confirmed by detailed modeling. The planetary anomaly was found in pure survey observations by the Optical Gravitational Lensing Experiment (OGLE; Udalski et al. 2015), i.e., the planet detection did not depend on a targeted follow-up photometry. This means that the planet can be included in future statistical studies of the wide-orbit planets. For OGLE-2012-BLG-0838, high-resolution imaging and satellite imaging were collected, which helps to directly constrain the planet properties.

In the next section, we present the data collected for OGLE-2012-BLG-0838. We describe the model fitting in Section 3. In Section 4, we analyze current constraints on the physical properties of the system. We summarize the paper in Section 5.

2. OBSERVATIONS

2.1. OGLE photometry

OGLE is a large scale photometric survey. It is currently in its fourth phase (OGLE-IV) and operates a 1.3-m telescope at Las Campanas Observatory (Chile) that is equipped with a 32-CCD chip camera (256M pixel in total). The camera field of view is 1.4 deg^2 , and the pixel scale is $0''.26$. OGLE bulge observations are performed in the I band, and we use only these to fit the microlensing model. When the anomaly occurred, the field of OGLE-2012-BLG-0838 was observed once per one or two nights. There are 20 OGLE fields that are observed with higher cadence. For the OGLE-2012-BLG-0838 field, the median seeing is $1''.4$, which is slightly higher than in other bulge fields. Additional lower cadence V -band data on the target exist, but do not cover the anomaly, and we use them only to characterize the source star. Photometry of the OGLE data is performed using difference image analysis (Alard 2000; Woźniak 2000). We corrected the native photometric uncertainties following Skowron et al. (2016). For a more detailed description of the OGLE survey, see Udalski et al. (2008) and Udalski et al. (2015).

The search for microlensing events in the OGLE data is performed daily (Udalski 2003). The event OGLE-2012-BLG-0838 was discovered on $\text{HJD}' \equiv \text{HJD} - 2450000 = 6082$, i.e., after the anomaly was over. The planetary nature of the anomaly was first suggested on $\text{HJD}' = 6126.403$ (by A. U.), and subsequently the planetary models were fitted (by C. H.). Event coordinates are R.A. = $18^{\text{h}}12^{\text{m}}00^{\text{s}}.74$ and Dec. = $-25^{\circ}42'41''.8$, which translate to $l = 5^{\circ}.720$ and $b = -3^{\circ}.472$. The baseline brightness in the standard photometric system is: $I = 17.610 \text{ mag}$ and $(V - I) = 1.851 \text{ mag}$ (Szymański et al. 2011).

2.2. EPOXI imaging

Thanks to the early recognition of its anomaly, OGLE-2012-BLG-0838 was scheduled for observations with the *EPOXI* mission, which is re-purposed *Deep Impact* spacecraft (Hampton et al. 2005). There are 6516 images collected between $\text{HJD}' = 6136$ and 6150. The *EPOXI* images are out-of-focus, and each star produces a donut-shaped image. In the dense stellar fields of the Galactic bulge, the images of many stars are overlapping, which hinders photometric analysis. Thus the OGLE-2012-BLG-0838 *EPOXI* data have not yet been reduced. For an analysis of *EPOXI* data for a different event, see Muraki et al. (2011).

2.3. VVV photometry

The Variables in the Via Lactea (VVV) survey (Minniti et al. 2010) observed the Galactic bulge between 2010 and 2015 using the near-infrared 4-m VISTA telescope situated at the Paranal Observatory (Chile). VVV took most of its observations in the K_s band. The event OGLE-2012-BLG-0838 is detectable in VVV data, but no useful data were taken during, or close to the anomaly. The epoch closest to the anomaly was secured under non-photometric conditions. Hence, the VVV K_s -band data do not usefully constrain the binary lens microlensing model, and we use them only to derive the source properties. Photometry was extracted using a PSF-fitting technique. From the VVV data we derive baseline $K_s = 15.190$ mag.

2.4. SMARTS photometry

Immediately following A. U.'s planetary alert (HJD' = 6126.403), the Microlensing Follow Up Network (μ FUN) initiated observations using the ANDICAM dual-beam optical-IR camera (DePoy et al. 2003) on the SMARTS 1.3m telescope at Cerro Tololo InterAmerican Observatory (CTIO, Chile). The sole purpose of these observations was to characterize the source, primarily to measure the H -band source flux in order to compare to possible future high-resolution adaptive optics imaging. During these H -band observations using the IR channel, the optical channel was used to obtain V and I data as back-up for the unlikely possibility of problems with the OGLE V -band data. However, as anticipated, there were no such problems. Hence, only the H -band data are used in the present analysis. Because the observations began before the main peak, they covered a complete range of magnifications from near-baseline to peak, which is the main guarantee for an accurate measurement of the source flux. The data were reduced using DoPhot (Schechter et al. 1993). The zero-point of the photometry was calibrated using 154 nearby stars with VVV photometry. The difference between VVV photometry and SMARTS instrumental magnitudes shows a linear dependence on the magnitude itself and we take this effect into account in the zero-point calibration. The calibration has uncertainty of 0.053 mag. There were a total of 205 H -band observations in ten-dither or five-dither groups at a total of 21 epoch, of which 150 observations were successfully reduced. Median seeing of SMARTS data is $1''.2$.

2.5. Magellan adaptive optics imaging

The H -band high-resolution images of the OGLE-2012-BLG-0838 field were taken on HJD' = 6766, with Magellan Adaptive Optics system (MagAO; Close et al. 2012; Males et al. 2014; Morzinski et al. 2014) on the 6.5-m Clay Telescope at Las Campanas Observatory (Chile). We used the Clio Wide camera, which has a plate scale of 27.49 mas and a field of view of $14'' \times 28''$. The integration time for an individual science exposure was 30 seconds, and we took ten sets of images with four dithers for each set. We performed the coordinate transformation from the OGLE frame to the MagAO frame using the positions of the six common isolated stars. The position of the source that we identify on MagAO image lies $(22, -14) \pm (19, 17)$ mas in the East and North relative to the transformed position of the target centroid on the subtracted OGLE image. The closest star on the MagAO images is about 390 mas away, so the identification of the target is secure. The MagAO source is isolated with a FWHM of 160 mas. We use SExtractor (Bertin & Arnouts 1996) to perform aperture photometry on the MagAO images. MagAO data are typically calibrated to the 2MASS photometric catalog (Skrutskie et al. 2006). Due to lack of overlapping stars between MagAO image of OGLE-2012-BLG-0838 and 2MASS catalog, we used the VVV data as a bridge between 2MASS and MagAO to do the

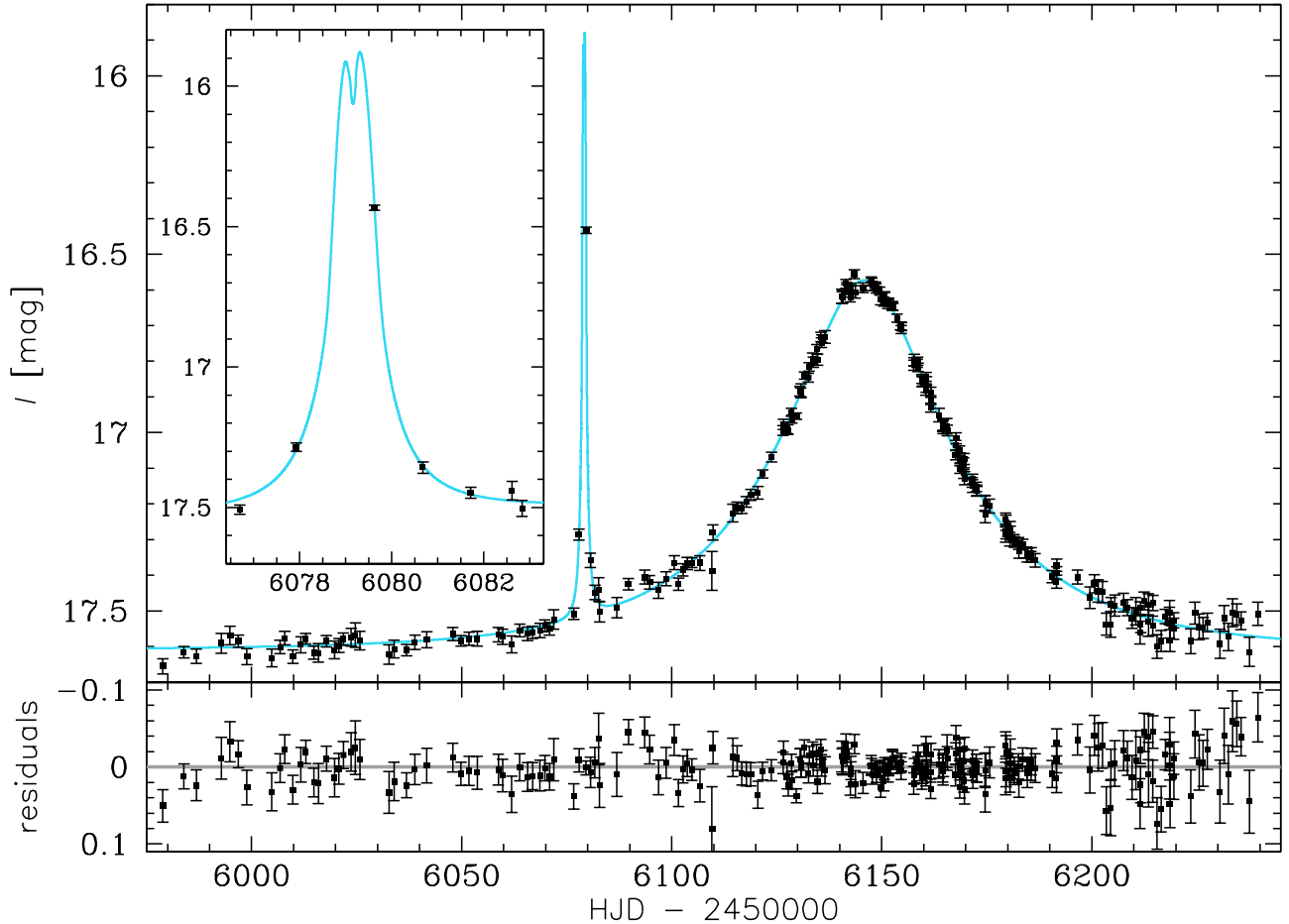


Figure 1. Light curve of OGLE-2012-BLG-0838 and the best-fitting model. The inset zooms-in on the anomaly. OGLE I band data are shown.

photometric calibration. We performed PSF photometry on the extracted VVV image with DoPhot (Schechter et al. 1993) and then we used common isolated stars within $3'$ of the target to calibrate it to the 2MASS magnitude system. Only stars with $H > 12.8$ mag are used to avoid detector non-linearity for VVV. Then we calibrated the MagAO magnitudes using four common isolated stars between MagAO and VVV.

3. MICROLENSING MODELS

The light curve of OGLE-2012-BLG-0838 (Figure 1) presents the main event, which is well-approximated by the Paczyński (1986) point-source point-lens model. The anomaly is short and high-amplitude, but its shape is not well determined. Such events can be produced by two types of events: 1) a binary source and a single lens or 2) a single source and a binary lens (Gaudi 1998). Furthermore, the binary lens case presents two possibilities (e.g., Bhattacharya et al. 2016; Poleski et al. 2018): separation s can be larger or smaller than one (called wide and close model, respectively). We discuss all three possibilities below, starting from the binary lens $s > 1$ (or wide solution), which turns out to be the correct model.

Table 1. Wide binary-lens models

Parameter	static model	parallax $u_0 > 0$	parallax $u_0 < 0$
		model	model
t_0	6145.935 ± 0.055	6146.07 ± 1.09	6145.84 ± 0.35
u_0	0.348 ± 0.015	0.356 ± 0.019	-0.361 ± 0.018
t_E (d)	42.4 ± 1.3	40.9 ± 1.5	40.9 ± 1.5
ρ	0.0067 ± 0.0022	0.0070 ± 0.0026	0.0071 ± 0.0026
$\pi_{E,N}$...	0.04 ± 0.36	-0.04 ± 0.39
$\pi_{E,E}$...	$-0.129^{+0.069}_{-0.114}$	$-0.125^{+0.050}_{-0.068}$
α (deg)	12.39 ± 0.19	12.18 ± 0.29	-12.37 ± 0.25
s	2.088 ± 0.040	2.138 ± 0.050	2.136 ± 0.049
q	$0.000400^{+0.000058}_{-0.000035}$	$0.000436^{+0.000073}_{-0.000045}$	$0.000442^{+0.000073}_{-0.000044}$
$F_s/(F_s + F_b)^a$	0.799 ± 0.046	0.835 ± 0.058	0.832 ± 0.054
$\chi^2/\text{d.o.f.}$	564.59/663	560.27/661	560.31/661

^a F_s is the source flux and F_b is the blending flux. Both are for the I band.

3.1. Wide binary-lens model

To represent a binary-lens model, we use following parameters: t_0 – the epoch of the minimum approach, u_0 – the minimum separation (normalized to θ_E), t_E – the Einstein timescale, ρ – the source radius (normalized to θ_E), α – the angle between the source trajectory and the lens axis, s , and q . For parameter conventions we follow Skowron et al. (2011) except for t_0 and u_0 , which are defined relative to the primary lens. The first three parameters (t_0 , u_0 , and t_E) are constrained by the main subevent, i.e., their values can be obtained by fitting a point-lens model to the data with the anomaly epochs removed. The other parameters are constrained by the time and length of the anomaly, and all except ρ can be relatively well estimated by visual inspection of the light curve. There are two additional flux parameters: the source flux and the blending flux. We estimate them separately for each model using linear regression. The linear limb-darkening coefficient is assumed to be $\Gamma = 0.46$, which was estimated based on a preliminary fitted model and the color-surface brightness relations by Claret & Bloemen (2011).

We first tried to fit the model using the frequently used Monte Carlo Markov chain (MCMC) technique. Multiple runs were carried out with a variety of settings: most importantly, the covariance matrix used for selecting candidate steps was modified. Yet, not a single run was well-mixed. The chains became trapped in narrow local minima and did not move out of them even after hundreds or thousands steps. We then used Multimodal Ellipsoidal Nested Sampling algorithm or MultiNest (Feroz & Hobson 2008; Feroz et al. 2009). At each step MultiNest approximates the probed distribution by a union of multidimensional ellipsoids. MultiNest fitted the model without any of the problems seen in MCMC. It turned out that the parameter space has a complicated shape that caused the usual MCMC technique to get stuck in local minima.

We present the results of the model fitting in the first column of Table 1 and in Figure 1. We report only a single mode there. The MultiNest can sample multimodal posterior and search for multiple

separated modes. The search for multiple modes can be run on all parameters or a selected subset of parameters. When we search for multiple modes on all parameters, only a single mode is found. When the search for multiple modes is run only on ρ , then 10-30 modes are found, depending on the exact settings. The 1σ ranges of the posterior parameters of these modes are overlapping, showing that available data do not allow unique identification of multiple modes. We inspected many models and present selected ones in Figure 2. Some models predict a light curve that differs significantly from the main model during the times not covered by the data. It seems likely that a few additional data points over the anomaly would pinpoint the model as was the case for OGLE-2008-BLG-092 (Poleski et al. 2014). On the other hand, with just a single point less, the anomaly shape would be much less constrained, similarly to the case of OGLE-2002-BLG-055 (Gaudi & Han 2004).

We derive the source brightness using posterior distributions. We obtain: $V_s = 19.697 \pm 0.063$ mag, $I_s = 17.853 \pm 0.062$ mag, $H_s = 15.582 \pm 0.063$ mag, and $K_{s,s} = 15.427 \pm 0.063$ mag.

After considering the static binary-lens model, we tried to include the microlensing parallax effect. It is described by a 2D vector $\boldsymbol{\pi}_E$, whose amplitude is equal to the relative lens-source parallax divided by θ_E . If both θ_E and $\boldsymbol{\pi}_E$ are measured, then both the lens mass (M) and distance (D_l) are measured directly (Gould 2000):

$$M = \frac{\theta_E}{\kappa\pi_E}, \quad \frac{1}{D_l} = \frac{\pi_E\theta_E}{\text{AU}} + \frac{1}{D_s}, \quad (1)$$

where $\kappa = 4G/(\text{AU}c^2) = 8.14 \text{ mas } M_\odot^{-1}$ is a constant, and D_s is the source distance. The annual microlensing parallax breaks the assumption that the source motion is rectilinear. The effect is undetectable for most events, because during their (typically short) duration, Earth's motion around the Sun can be well approximated by a straight line. OGLE-2012-BLG-0838 has relatively long t_E of 40 days. The anomaly additionally increases the chances of measuring π_E , because it provides a well-timed event (An & Gould 2001). To fully define the parallax model, one has to specify $t_{0,\text{par}}$ – i.e., the parameter reference time (Skowron et al. 2011). This is used to define inertial frame, and a frequent choice is $t_{0,\text{par}} \approx t_0$. Here, we adopt $t_{0,\text{par}} = 6080$, i.e., during the time that constrains the ρ measurement.

We consider two degenerate scenarios: $u_0 < 0$ and $u_0 > 0$. The models are presented in the last two columns of Table 1. Only the East component of $\boldsymbol{\pi}_E$ is measured at 1.9σ ($u_0 > 0$) and 2.5σ ($u_0 < 0$) significance and $\pi_{E,N}$ is basically unconstrained.

The annual microlensing parallax can be mimicked by the lens orbital motion (Batista et al. 2011; Skowron et al. 2011). We have fitted the models with parallax and instantaneous lens orbital motion, which is represented by two additional parameters: $d\alpha/dt$ and ds/dt . We applied following priors: $|d\alpha/dt| < 2 \text{ rad yr}^{-1}$, $|ds/dt| < 4 \text{ yr}^{-1}$, and $10^{-4} < \rho < 0.02$. From the posterior distribution we remove the models for which the ratio of kinetic to potential projected energy $E_{\perp,\text{kin}}/E_{\perp,\text{pot}}$ (see Dong et al. 2009; Batista et al. 2011, calculated assuming $D_s = 8 \text{ kpc}$) is greater than one, i.e., these models are unbound. We have considered only the $u_0 > 0$ solution and have run extensive simulations. The best bound model improves χ^2 by 2.15 compared to the parallax model and has $E_{\perp,\text{kin}}/E_{\perp,\text{pot}} = 0.93$. Such large value of the ratio of projected energy is unlikely, even though it is not forbidden. For smaller values of $E_{\perp,\text{kin}}/E_{\perp,\text{pot}}$, the χ^2 improvement is not significant: $\Delta\chi^2 = 1.07$ for $E_{\perp,\text{kin}}/E_{\perp,\text{pot}} < 0.5$ and $\Delta\chi^2 = 0.18$ for $E_{\perp,\text{kin}}/E_{\perp,\text{pot}} < 0.25$. The $\boldsymbol{\pi}_E$ mean value changes by less than 0.4σ and uncertainties do not change by more than 10%, hence, we conclude that the lens orbital motion does not significantly affect the parallax measurement.

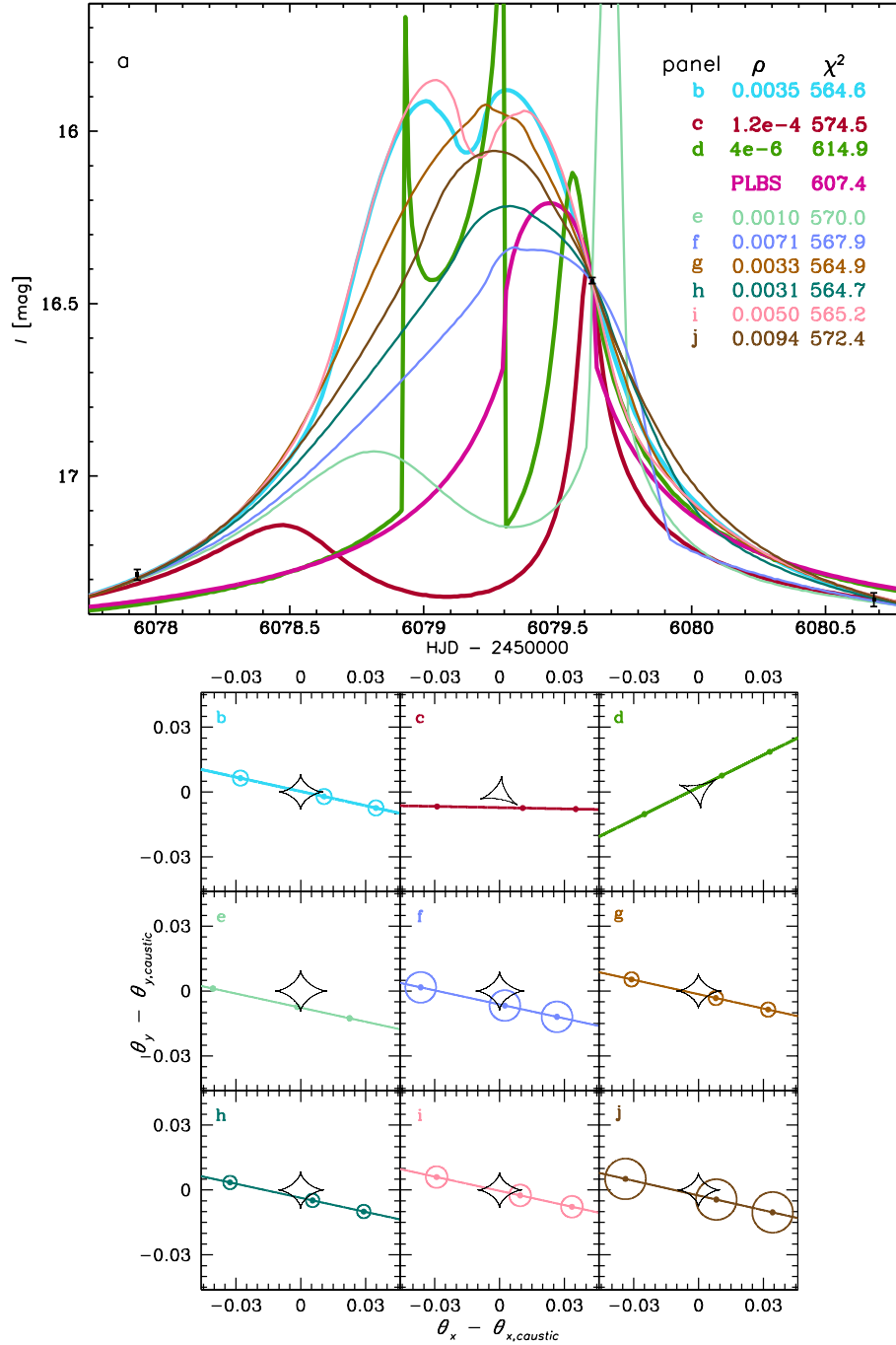


Figure 2. Degenerate microlensing models for OGLE-2012-BLG-0838. *The upper panel (a)* presents model light curves and three data points (black; at 6077.9, 6079.6, and 6080.7) that constrain the anomalous part of the model. The thicker lines represent four main models (wide, close A, close B, and binary-source). The remaining models are all wide binary-lens models and were selected from the search for multiple modes run only on ρ . The legend gives ρ and χ^2 values for each model. Two models peak beyond the plot at (6079.3, 13.55) and (6079.7, 15.20). *The lower panels (b-j)* show the corresponding trajectories and planetary caustics (black) for the binary-lens models. The colored circles represent the size of the source as well as its position at the times that the data were taken. The source is moving from left to right. The coordinate system is centered on a planetary caustic. In *panels (c) and (d)*, the two triangular caustics correspond to close models. In this coordinate systems, the central caustics are at (1.56, -0.38) and (1.57, 0.38), respectively. For the other models (i.e., wide), the primary is at (≈ 1.6 , 0). For the three models with $\rho < 0.002$ (*panels c, d, and e*), the actual source size is smaller than the points shown.

3.2. Close binary-lens model

We additionally searched for close (i.e., $s < 1$) binary-lens models. The best-fitting model has $\rho = 0.00142 \pm 0.00051$, $\alpha = 178.54 \pm 0.63$ deg, $s = 0.4832 \pm 0.0079$, $q = 0.0113 \pm 0.0013$, and $\chi^2 = 574.47$, i.e., it is worse fit to the data by $\Delta\chi^2 = 10$. It is also presented in panels *a* and *c* of Figure 2. We have compared Bayesian evidence for this model and the wide-binary lens model. We assumed a log-uniform prior in s and q and a uniform prior in other parameters. The likelihood ratio is $\mathcal{L}_{\text{wide}}/\mathcal{L}_{\text{close}} = 18847$, which strongly prefers the wide solution. The a priori probability also favors the wide model over the close one. Recent statistical analysis of microlensing events (Suzuki et al. 2016) shows that the microlensing planet occurrence rate is increasing with increasing s and decreasing q , and this result is confirmed by joint analysis of microlensing, radial velocity, and direct imaging results (Clanton & Gaudi 2016). In the present case, the Suzuki et al. (2016) planet occurrence rate $d^2N/(d \log s d \log q)$ favors the wide model by a factor of 45.8. We reject the close model based on the two arguments given above.

The close model with $\alpha = 179$ deg has a source trajectory that crosses the binary axis outside the caustics (in other words, the source passes all caustics on the same side). There is a second model in which the source trajectory crosses the binary axis between the planetary and central caustics (Poleski et al. 2018). See panels *a* and *d* of Figure 2. For OGLE-2012-BLG-0838, the latter model has $\alpha = 206.65 \pm 0.68$ deg and a corresponding χ^2 is 614.94, i.e., large enough to reject this model.

3.3. Binary-source model

The binary-source model introduces three additional parameters as compared to the point-source point-lens model ($t_{0,2}$, $u_{0,2}$ and flux ratio of two sources). The best binary-source model is presented in Figure 2 (see PLBS model) and has χ^2 of 607.35, i.e., worse by 42.8 than the wide binary-lens model. Clearly, the wide binary-lens model fits the data better, and we reject the binary-source model.

4. SYSTEM PROPERTIES

Here we discuss a few different pieces of information about the lens and source. We are not able to directly measure the lens mass and distance, but we discuss the prospects for doing so. Thus, at the end of this section we derive the lens properties instead using Bayesian priors derived using a Galactic simulation.

In Figure 3, we show the MagAO image of OGLE-2016-BLG-0838. The final calibrated *H*-band brightness of the target is $H_{\text{target}} = 15.29 \pm 0.05$ mag, where the error estimate combines the statistical and systematic errors. H_{target} is brighter than the *H*-band source flux measured before and the difference corresponds to $H_{\text{excess}} = 16.86 \pm 0.30$ mag. We may estimate the probability that H_{excess} comes from a star not related to the event. We measure the density of stars brighter than H_{excess} from VVV catalog and after correcting for slight incompleteness at the faintest magnitudes obtain $0.152 \text{ arcsec}^{-2}$. The MagAO image would not reveal H_{excess} star if it were closer than 1.4 FWHM to the target, which corresponds to the sky area of 0.16 arcsec^2 . The expected number of unrelated stars that could not be resolved is thus $0.152 \text{ arcsec}^{-2} \times 0.16 \text{ arcsec}^2 = 0.024 \ll 1$, hence, most likely H_{excess} comes from the lens, the lens companion, the source companion, or their combination.

The relative lens-source proper motion is: $\mu_{\text{rel}} = \theta_{\text{E}}/t_{\text{E}} = 3 \text{ mas yr}^{-1}$ (see below). We may expect that the lens and source could be resolved in about ten years from now and the lens flux could be measured then leading to the lens mass and distance estimate, when combined with the stellar

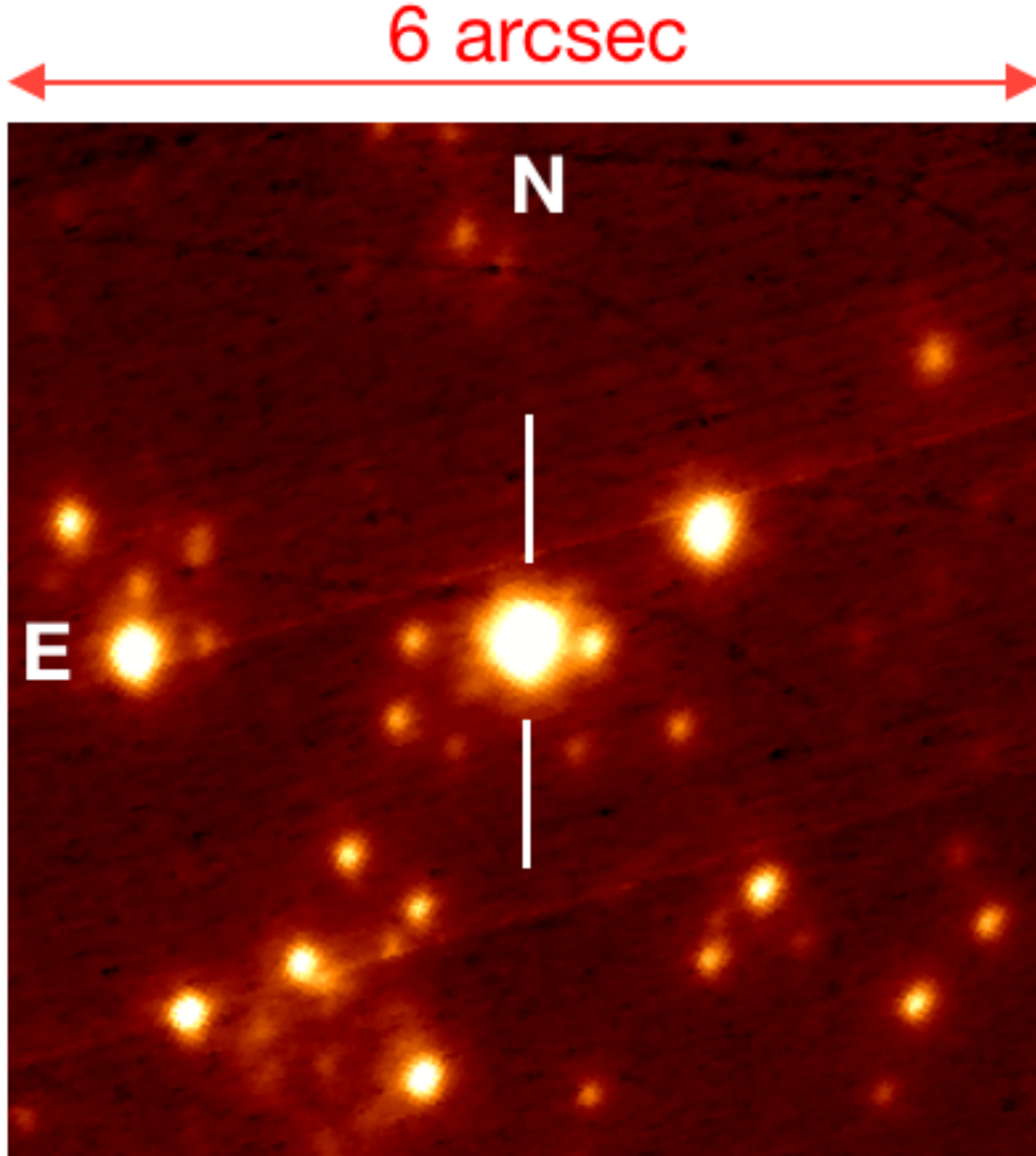


Figure 3. MagAO image of target field. The star is primarily due to OGLE-2012-BLG-0838 source star.

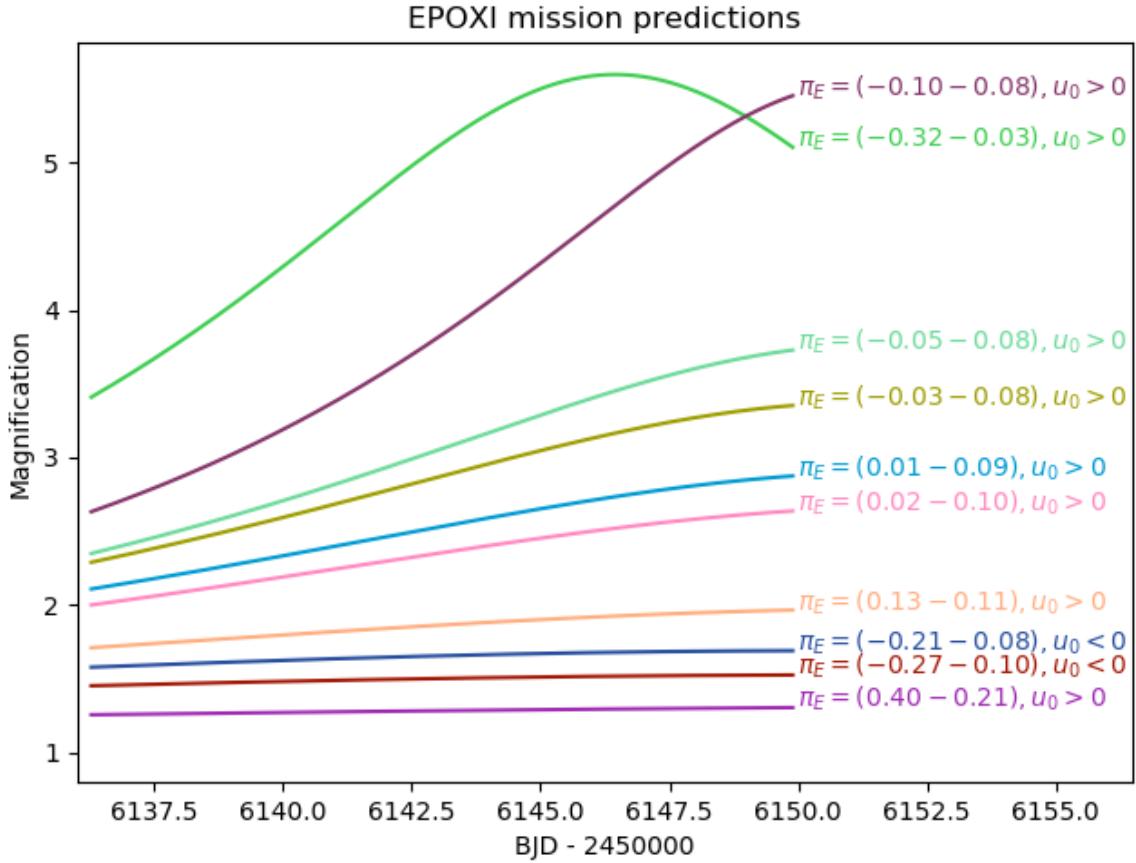
isochrones (Yee 2015). In some cases, an identification of the lens in the follow-up high-resolution imaging is problematic (Bhattacharya et al. 2017). The future lens flux measurement can definitely use the MagAO image presented here for calibration. We also list nearby stars in Table 2. As one can see in Figure 3, the event is by far the brightest object within the ground-based seeing limit.

The existing *EPOXI* data have not yet been reduced. We use representative models from Section 3.1 to predict the magnification as seen by *EPOXI* – see Figure 4. We also show a histogram of the amplitude (i.e., difference between maximum and minimum) of magnification predicted for *EPOXI* in Figure 5. The lens mass and distance can be measured directly if the microlensing parallax is measured. Some of the magnification curves are almost flat. If the true magnification curve is

Table 2. Stars detected close to the target on MagAO image

No.	distance [arcsec]	$\Delta\alpha \cos \delta$ [arcsec]	$\Delta\delta$ [arcsec]	H [mag]
1	0.39	-0.379	-0.026	17.474 ± 0.060
2	0.64	0.644	0.003	18.073 ± 0.084
3	0.87	0.742	-0.449	18.174 ± 0.070
4	1.02	-0.884	-0.501	18.469 ± 0.073
5	1.24	-1.056	0.652	16.307 ± 0.053

NOTE— $\Delta\alpha \cos \delta$ and $\Delta\delta$ indicate the displacement from the target along R.A. and Dec. directions, respectively.


Figure 4. Representative magnification curves predicted for *EPOXI*.

almost flat, then the parallax measurement is unlikely. If the highest magnification is $\lesssim 4$, then the magnification curve can be approximated as a linear function of time. In this case, it will be necessary to remove potential systematic linear trends in the *EPOXI* photometry in a manner that is independent of the photometry of the source in the *EPOXI* data in order to measure π_E .

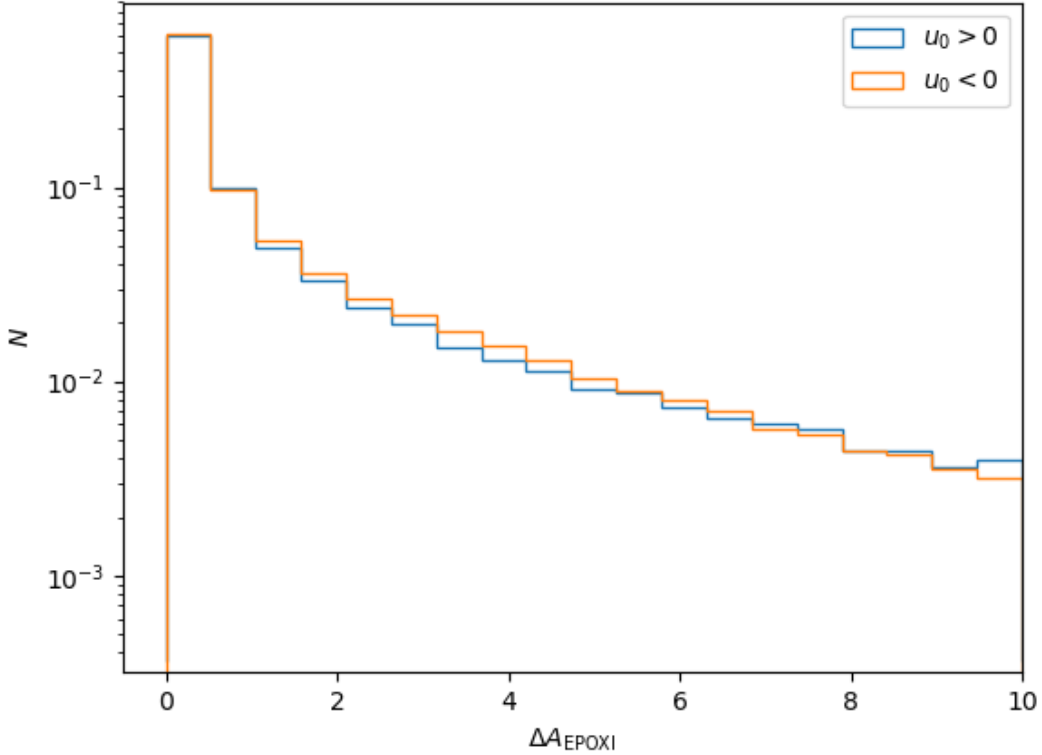


Figure 5. Histogram of the predicted magnification amplitude for *EPOXI*. The ΔA_{EPOXI} values larger than 10 are not excluded but have very low probability.

To measure θ_E , we use the method developed by Yoo et al. (2004). We present the color-magnitude diagram of stars lying within $2'$ from the target in Figure 6. The red clump has an observed color $(V - I)_{\text{RC}} = 2.003 \pm 0.008$ mag and brightness $I_{\text{RC}} = 15.489 \pm 0.030$ mag. We compare these values with the extinction-corrected values from Bensby et al. (2011) and Nataf et al. (2013) to obtain $E(V - I) = 0.943$ mag and $A_I = 1.157$ mag. The extinction-corrected source properties are $I_{s,0} = 16.696$ mag and $V_{s,0} = 17.523$ mag and using the Bessell & Brett (1988) color-color relations we obtain $(V - K)_{s,0} = 1.801$ mag. The estimated $(V - K)_{s,0}$ and $V_{s,0}$ correspond to $\theta_* = 1.85 \pm 0.14 \mu\text{as}$ (Kervella et al. 2004). When combined with ρ for static wide model we obtain $\theta_E = 0.319_{-0.089}^{+0.275}$ mas.

We have placed only weak constraint on the microlensing parallax, hence, we have to use Bayesian simulations of the Galaxy to derive the lens mass and distance. For this purpose, we use an approach presented by Clanton & Gaudi (2014). In short, the lenses are the main sequence stars drawn from the density profiles of a double-exponential disc and the boxy Gaussian bulge. The main sequence mass function is taken from the model 1 in Sumi et al. (2011). For source distance we use the boxy Gaussian bulge distribution, i.e., model G2 by Dwek et al. (1995). The results of the simulations are presented in Table 3. We run the simulation twice: first, for the static model, and second, imposing parallax constraint from Table 1. Adding the parallax constraint slightly reduces μ_{rel} and increases D_l and M_l . In either case, we infer that the lens is a low-mass star, as expected.

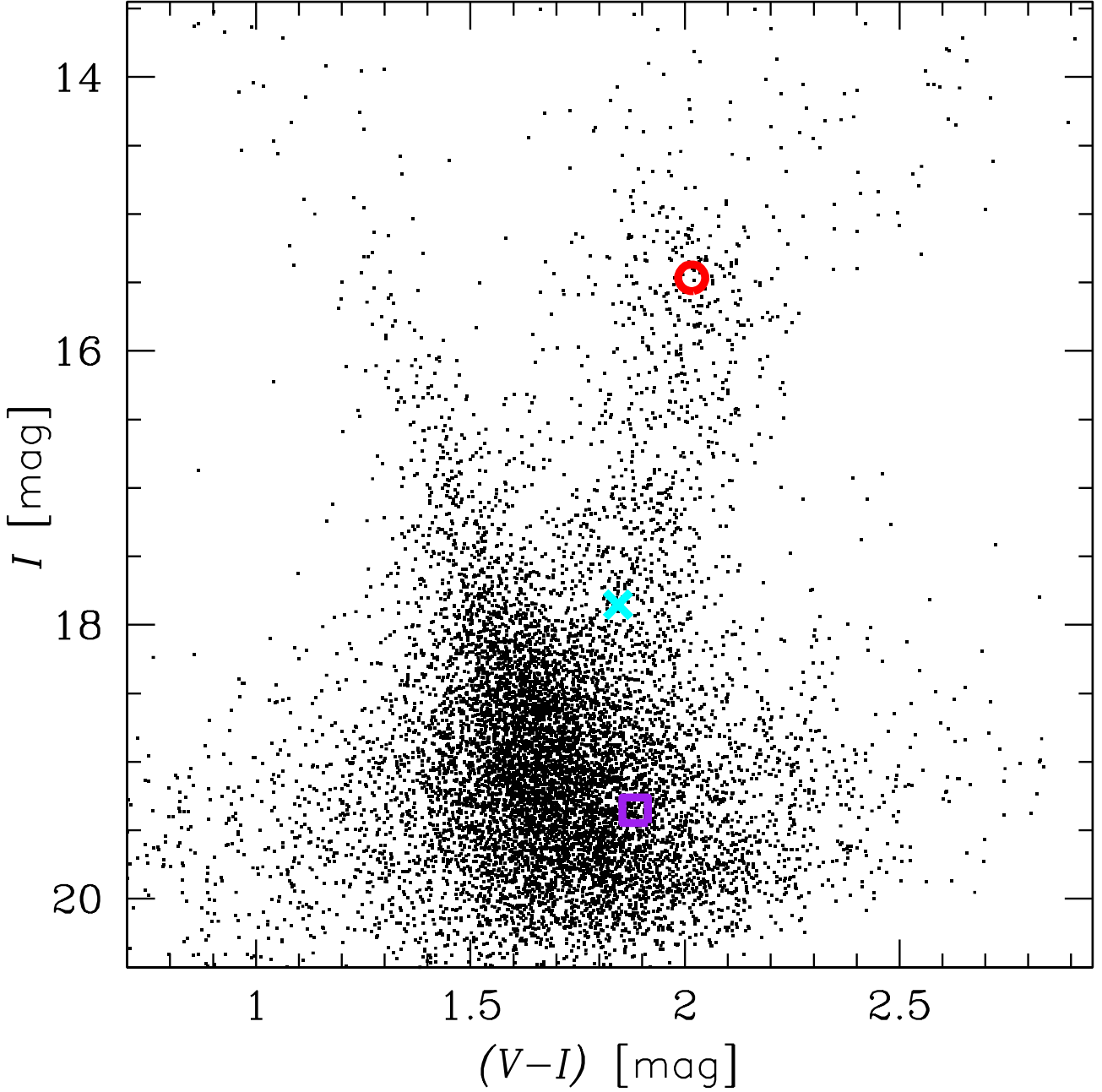


Figure 6. Color-magnitude diagram for stars within $2'$ around the target. The cross marks the source position as derived from the posterior distribution. The red circle indicates the red clump and the purple square marks the blending light ($I_b = 19.35 \pm 0.25$ mag, $(V - I)_b = 1.88 \pm 0.31$ mag). Standard photometric system is used (Szymański et al. 2011).

Table 3 gives our prediction of the lens mass and distance. These quantities allow us to estimate the brightness of the lens and compare it to the blending light. For the fiducial value $M_l = 0.42 M_\odot$, the absolute brightness of the lens would be $M_I = 7.8$ mag (Dotter et al. 2008) assuming $[\text{Fe}/\text{H}] = -1$ and age of 10 Gyr. At D_l of 6 kpc, the lens is almost certainly behind almost all of the dust. Hence, the

Table 3. Posterior Physical Parameters Statistics

Parameter	unit	static model	parallax model
μ_{rel}	mas yr ⁻¹	$3.06^{+1.72}_{-0.85}$	$2.70^{+1.05}_{-0.66}$
D_s	kpc	7.90 ± 0.93	7.92 ± 0.88
D_l	kpc	$5.9^{+1.1}_{-1.6}$	6.62 ± 0.85
M_l	M _⊙	$0.42^{+0.29}_{-0.21}$	0.54 ± 0.25
M_p	M _{Jup.}	$0.18^{+0.124}_{-0.088}$	0.25 ± 0.12
r_E^a	AU	$1.98^{+0.69}_{-0.50}$	$1.96^{+0.62}_{-0.46}$
r_{\perp}^b	AU	$4.1^{+1.5}_{-1.1}$	$4.2^{+1.4}_{-1.0}$

^aEinstein ring radius projected on lens plane: $r_E = D_l \theta_E$.

^bInstantaneous projected star-planet separation: $r_{\perp} = s D_l \theta_E$.

lens extinction should be similar to the source extinction. Combining all these pieces of information, we may expect the lens brightness of 22.8 mag i.e., 3.5 mag fainter than the light blended with the source. For $M_l = 0.75 M_{\odot}$ and the same distance, the lens brightness is only 0.24 mag fainter than the light blended with the source.

We can also estimate the H -band lens brightness and compare it to H_{excess} . From H vs. $(I - H)$ color-magnitude diagram and the intrinsic red clump color from [Nataf et al. \(2016\)](#) we estimate $A_H = 0.27$ mag. For $M_l = 0.42 M_{\odot}$ the absolute H -band brightness is 6.2 mag and the estimated lens brightness $H_l = 20.4$ mag. For $M_l = 0.75 M_{\odot}$ we obtain $H_l = 18.0$ mag and both H_l values are significantly fainter than $H_{\text{excess}} = 16.86 \pm 0.30$ mag.

We can estimate the expected RV signal from OGLE-2012-BLG-0838Lb. We estimate the semi-major axis: $a = (3/2)^{1/2} r_{\perp} = 5.0$ AU. For $M_l = 0.42 M_{\odot}$ the orbital period is $P = (a^3/M)^{1/2} = 17.4$ yr. For the edge-on configuration, the RV signal would be $K = 3.4$ m s⁻¹. Detecting planets with similar properties around nearby stars is challenging for the RV surveys. The longest period RV planets with well-measured RV curves are HD 30177c (20.8 yr or 31.8 yr; [Wittenmyer et al. 2017](#)) and GJ 676Ac (20.4 yr; [Sahlmann et al. 2016](#)), though for neither of them the RV data cover the full orbital period.

5. SUMMARY

We have presented the microlensing discovery of a wide-orbit planet OGLE-2012-BLG-0838Lb. Alternative models of observed light curve were considered and found inadequate. Finding planets on similar orbits around low-mass stars presents a challenge. The lens physical properties are constrained but not directly measured. We discuss here additional existing and future data that can constrain the physical parameters of the lens system directly.

OGLE Team acknowledges Marcin Kubiak and Grzegorz Pietrzyński, former members of the team, for their contribution to the collection of the OGLE photometric data over the past years. We thank Michael Albrow for information about the *EPOXI* observations. We thank Ping Chen and Ji Wang for their help. This work was supported by NASA contract NNG16PJ32C. The OGLE project has received funding from the National Science Centre, Poland, grant MAESTRO 2014/14/A/ST9/00121

to A. U. Work by C. H. was supported by the grant (2017R1A4A1015178) of National Research Foundation of Korea. This paper includes data gathered with the 6.5-m Magellan Clay Telescope at Las Campanas Observatory, Chile. X. X. and S. D. acknowledge Project 11573003 supported by NSFC. This research uses data obtained through the Telescope Access Program (TAP), which has been funded by “the Strategic Priority Research Program-The Emergence of Cosmological Structures” of the Chinese Academy of Sciences (Grant No.11 XDB09000000) and the Special Fund for Astronomy from the Ministry of Finance. Work by A. G. was supported by AST-1516842 from the US NSF and by JPL grant 1500811. A. G. received support from the European Research Council under the European Union’s Seventh Framework Programme (FP 7) ERC Grant Agreement n. [321035]. Based on data products from observations made with ESO Telescopes at the La Silla Paranal Observatory under programme ID 179.B-2002.

Software: Astropy (Astropy Collaboration et al. 2013, 2018), SExtractor (Bertin & Arnouts 1996), DoPhot (Schechter et al. 1993), MulensModel (Poleski & Yee 2018, 2019), <https://arxiv.org/src/1408.6223v3/anc>, MultiNest (Feroz & Hobson 2008; Feroz et al. 2009), Numerical Recipes (Press et al. 1992), SM <https://www.astro.princeton.edu/~rhl/sm/>, AstroML (Ivezić et al. 2014)

REFERENCES

- Alard, C. 2000, *A&AS*, 144, 363, doi: [10.1051/aas:2000214](https://doi.org/10.1051/aas:2000214)
- An, J. H., & Gould, A. 2001, *ApJL*, 563, L111, doi: [10.1086/338657](https://doi.org/10.1086/338657)
- Astropy Collaboration, Robitaille, T. P., Tollerud, E. J., et al. 2013, *A&A*, 558, A33, doi: [10.1051/0004-6361/201322068](https://doi.org/10.1051/0004-6361/201322068)
- Astropy Collaboration, Price-Whelan, A. M., Sipőcz, B. M., et al. 2018, *AJ*, 156, 123, doi: [10.3847/1538-3881/aabc4f](https://doi.org/10.3847/1538-3881/aabc4f)
- Batista, V., Gould, A., Dieters, S., et al. 2011, *A&A*, 529, A102, doi: [10.1051/0004-6361/201016111](https://doi.org/10.1051/0004-6361/201016111)
- Beichman, C. A., Giles, H. A. C., Akeson, R., et al. 2018, *AJ*, 155, 158, doi: [10.3847/1538-3881/aaab6](https://doi.org/10.3847/1538-3881/aaab6)
- Bensby, T., Adén, D., Meléndez, J., et al. 2011, *A&A*, 533, A134, doi: [10.1051/0004-6361/201117059](https://doi.org/10.1051/0004-6361/201117059)
- Bertin, E., & Arnouts, S. 1996, *A&AS*, 117, 393, doi: [10.1051/aas:1996164](https://doi.org/10.1051/aas:1996164)
- Bessell, M. S., & Brett, J. M. 1988, *PASP*, 100, 1134, doi: [10.1086/132281](https://doi.org/10.1086/132281)
- Bhattacharya, A., Bennett, D. P., Bond, I. A., et al. 2016, *AJ*, 152, 140, doi: [10.3847/0004-6256/152/5/140](https://doi.org/10.3847/0004-6256/152/5/140)
- Bhattacharya, A., Bennett, D. P., Anderson, J., et al. 2017, *AJ*, 154, 59, doi: [10.3847/1538-3881/aa7b80](https://doi.org/10.3847/1538-3881/aa7b80)
- Bowler, B. P. 2016, *PASP*, 128, 102001, doi: [10.1088/1538-3873/128/968/102001](https://doi.org/10.1088/1538-3873/128/968/102001)
- Cassan, A., Kubas, D., Beaulieu, J.-P., et al. 2012, *Nature*, 481, 167, doi: [10.1038/nature10684](https://doi.org/10.1038/nature10684)
- Chauvin, G., Lagrange, A.-M., Dumas, C., et al. 2004, *A&A*, 425, L29, doi: [10.1051/0004-6361:200400056](https://doi.org/10.1051/0004-6361:200400056)
- Clanton, C., & Gaudi, B. S. 2014, *ApJ*, 791, 90, doi: [10.1088/0004-637X/791/2/90](https://doi.org/10.1088/0004-637X/791/2/90)
- . 2016, *ApJ*, 819, 125, doi: [10.3847/0004-637X/819/2/125](https://doi.org/10.3847/0004-637X/819/2/125)
- Claret, A., & Bloemen, S. 2011, *A&A*, 529, A75, doi: [10.1051/0004-6361/201116451](https://doi.org/10.1051/0004-6361/201116451)
- Close, L. M., Males, J. R., Kopon, D. A., et al. 2012, in *Proc. SPIE*, Vol. 8447, Adaptive Optics Systems III, 84470X, doi: [10.1117/12.926545](https://doi.org/10.1117/12.926545)
- Coughlin, J. L., Mullally, F., Thompson, S. E., et al. 2016, *ApJS*, 224, 12, doi: [10.3847/0067-0049/224/1/12](https://doi.org/10.3847/0067-0049/224/1/12)
- DePoy, D. L., Atwood, B., Belville, S. R., et al. 2003, 4841, 827, doi: [10.1117/12.459907](https://doi.org/10.1117/12.459907)
- Dong, S., Gould, A., Udalski, A., et al. 2009, *ApJ*, 695, 970, doi: [10.1088/0004-637X/695/2/970](https://doi.org/10.1088/0004-637X/695/2/970)
- Dotter, A., Chaboyer, B., Jevremović, D., et al. 2008, *ApJS*, 178, 89, doi: [10.1086/589654](https://doi.org/10.1086/589654)
- Dwek, E., Arendt, R. G., Hauser, M. G., et al. 1995, *ApJ*, 445, 716, doi: [10.1086/175734](https://doi.org/10.1086/175734)
- Feroz, F., & Hobson, M. P. 2008, *MNRAS*, 384, 449, doi: [10.1111/j.1365-2966.2007.12353.x](https://doi.org/10.1111/j.1365-2966.2007.12353.x)

- Feroz, F., Hobson, M. P., & Bridges, M. 2009, *MNRAS*, 398, 1601, doi: [10.1111/j.1365-2966.2009.14548.x](https://doi.org/10.1111/j.1365-2966.2009.14548.x)
- Gaudi, B. S. 1998, *ApJ*, 506, 533, doi: [10.1086/306256](https://doi.org/10.1086/306256)
- Gaudi, B. S., & Han, C. 2004, *ApJ*, 611, 528, doi: [10.1086/421971](https://doi.org/10.1086/421971)
- Gaudi, B. S., Stassun, K. G., Collins, K. A., et al. 2017, *Nature*, 546, 514, doi: [10.1038/nature22392](https://doi.org/10.1038/nature22392)
- Gould, A. 2000, *ApJ*, 542, 785, doi: [10.1086/317037](https://doi.org/10.1086/317037)
- Gould, A., Dong, S., Gaudi, B. S., et al. 2010, *ApJ*, 720, 1073, doi: [10.1088/0004-637X/720/2/1073](https://doi.org/10.1088/0004-637X/720/2/1073)
- Hampton, D. L., Baer, J. W., Huisjen, M. A., et al. 2005, *SSRv*, 117, 43, doi: [10.1007/s11214-005-3390-8](https://doi.org/10.1007/s11214-005-3390-8)
- Hwang, K.-H., Ryu, Y.-H., Kim, H.-W., et al. 2019, *AJ*, 157, 23, doi: [10.3847/1538-3881/aaf16e](https://doi.org/10.3847/1538-3881/aaf16e)
- Ivezić, Ž., Connolly, A., Vanderplas, J., & Gray, A. 2014, *Statistics, Data Mining and Machine Learning in Astronomy* (Princeton University Press)
- Kane, S. R. 2011, *Icarus*, 214, 327, doi: [10.1016/j.icarus.2011.04.023](https://doi.org/10.1016/j.icarus.2011.04.023)
- Kervella, P., Bersier, D., Mourard, D., et al. 2004, *A&A*, 428, 587, doi: [10.1051/0004-6361:20041416](https://doi.org/10.1051/0004-6361:20041416)
- Kipping, D. M., Torres, G., Henze, C., et al. 2016, *ApJ*, 820, 112, doi: [10.3847/0004-637X/820/2/112](https://doi.org/10.3847/0004-637X/820/2/112)
- Kostov, V. B., Orosz, J. A., Welsh, W. F., et al. 2016, *ApJ*, 827, 86, doi: [10.3847/0004-637X/827/1/86](https://doi.org/10.3847/0004-637X/827/1/86)
- Males, J. R., Close, L. M., Morzinski, K. M., et al. 2014, *ApJ*, 786, 32, doi: [10.1088/0004-637X/786/1/32](https://doi.org/10.1088/0004-637X/786/1/32)
- Minniti, D., Lucas, P. W., Emerson, J. P., et al. 2010, *NewA*, 15, 433, doi: [10.1016/j.newast.2009.12.002](https://doi.org/10.1016/j.newast.2009.12.002)
- Morzinski, K. M., Close, L. M., Males, J. R., et al. 2014, 9148, 914804, doi: [10.1117/12.2057048](https://doi.org/10.1117/12.2057048)
- Mróz, P., Udalski, A., Skowron, J., et al. 2017, *Nature*, 548, 183, doi: [10.1038/nature23276](https://doi.org/10.1038/nature23276)
- Mróz, P., Ryu, Y.-H., Skowron, J., et al. 2018, *AJ*, 155, 121, doi: [10.3847/1538-3881/aaaae9](https://doi.org/10.3847/1538-3881/aaaae9)
- Muraki, Y., Han, C., Bennett, D. P., et al. 2011, *ApJ*, 741, 22, doi: [10.1088/0004-637X/741/1/22](https://doi.org/10.1088/0004-637X/741/1/22)
- Nataf, D. M., Gould, A., Fouqué, P., et al. 2013, *ApJ*, 769, 88, doi: [10.1088/0004-637X/769/2/88](https://doi.org/10.1088/0004-637X/769/2/88)
- Nataf, D. M., Gonzalez, O. A., Casagrande, L., et al. 2016, *MNRAS*, 456, 2692, doi: [10.1093/mnras/stv2843](https://doi.org/10.1093/mnras/stv2843)
- Paczynski, B. 1986, *ApJ*, 304, 1, doi: [10.1086/164140](https://doi.org/10.1086/164140)
- Perryman, M., Hartman, J., Bakos, G. Á., & Lindegren, L. 2014, *ApJ*, 797, 14, doi: [10.1088/0004-637X/797/1/14](https://doi.org/10.1088/0004-637X/797/1/14)
- Poleski, R., & Yee, J. 2018, <https://ascl.net/1803.006>
- Poleski, R., & Yee, J. C. 2019, *Astronomy and Computing*, 26, 35, doi: [10.1016/j.ascom.2018.11.001](https://doi.org/10.1016/j.ascom.2018.11.001)
- Poleski, R., Skowron, J., Udalski, A., et al. 2014, *ApJ*, 795, 42, doi: [10.1088/0004-637X/795/1/42](https://doi.org/10.1088/0004-637X/795/1/42)
- Poleski, R., Gaudi, B. S., Udalski, A., et al. 2018, *AJ*, 156, 104, doi: [10.3847/1538-3881/aad45e](https://doi.org/10.3847/1538-3881/aad45e)
- Press, W. H., Teukolsky, S. A., Vetterling, W. T., & Flannery, B. P. 1992, *Numerical recipes in FORTRAN. The art of scientific computing*
- Quintana, E. V., Barclay, T., Raymond, S. N., et al. 2014, *Science*, 344, 277, doi: [10.1126/science.1249403](https://doi.org/10.1126/science.1249403)
- Sahlmann, J., Lazorenko, P. F., Ségransan, D., et al. 2016, *A&A*, 595, A77, doi: [10.1051/0004-6361/201628854](https://doi.org/10.1051/0004-6361/201628854)
- Schechter, P. L., Mateo, M., & Saha, A. 1993, *PASP*, 105, 1342, doi: [10.1086/133316](https://doi.org/10.1086/133316)
- Shvartzvald, Y., Yee, J. C., Calchi Novati, S., et al. 2017, *ApJL*, 840, L3, doi: [10.3847/2041-8213/aa6d09](https://doi.org/10.3847/2041-8213/aa6d09)
- Skowron, J., Udalski, A., Gould, A., et al. 2011, *ApJ*, 738, 87, doi: [10.1088/0004-637X/738/1/87](https://doi.org/10.1088/0004-637X/738/1/87)
- Skowron, J., Udalski, A., Kozłowski, S., et al. 2016, *AcA*, 66, 1, <https://arxiv.org/abs/1604.01966>
- Skrutskie, M. F., Cutri, R. M., Stiening, R., et al. 2006, *AJ*, 131, 1163, doi: [10.1086/498708](https://doi.org/10.1086/498708)
- Snellen, I. A. G., & Brown, A. G. A. 2018, *Nature Astronomy*, 2, 883, doi: [10.1038/s41550-018-0561-6](https://doi.org/10.1038/s41550-018-0561-6)
- Sumi, T., Kamiya, K., Bennett, D. P., et al. 2011, *Nature*, 473, 349, doi: [10.1038/nature10092](https://doi.org/10.1038/nature10092)
- Suzuki, D., Bennett, D. P., Sumi, T., et al. 2016, *ApJ*, 833, 145, doi: [10.3847/1538-4357/833/2/145](https://doi.org/10.3847/1538-4357/833/2/145)

- Szymański, M. K., Udalski, A., Soszyński, I., et al. 2011, *AcA*, 61, 83.
<https://arxiv.org/abs/1107.4008>
- Udalski, A. 2003, *AcA*, 53, 291
- Udalski, A., Szymański, M. K., Soszyński, I., & Poleski, R. 2008, *AcA*, 58, 69.
<https://arxiv.org/abs/0807.3884>
- Udalski, A., Szymański, M. K., & Szymański, G. 2015, *AcA*, 65, 1.
<https://arxiv.org/abs/1504.05966>
- Udalski, A., Ryu, Y.-H., Sajadian, S., et al. 2018, *AcA*, 68, 1. <https://arxiv.org/abs/1802.02582>
- Winn, J. N., Matthews, J. M., Dawson, R. I., et al. 2011, *ApJL*, 737, L18,
doi: [10.1088/2041-8205/737/1/L18](https://doi.org/10.1088/2041-8205/737/1/L18)
- Wittenmyer, R. A., Horner, J., Mengel, M. W., et al. 2017, *AJ*, 153, 167,
doi: [10.3847/1538-3881/aa5f17](https://doi.org/10.3847/1538-3881/aa5f17)
- Wolszczan, A., & Frail, D. A. 1992, *Nature*, 355, 145, doi: [10.1038/355145a0](https://doi.org/10.1038/355145a0)
- Woźniak, P. R. 2000, *AcA*, 50, 421
- Yee, J. C. 2015, *ApJL*, 814, L11,
doi: [10.1088/2041-8205/814/1/L11](https://doi.org/10.1088/2041-8205/814/1/L11)
- Yoo, J., DePoy, D. L., Gal-Yam, A., et al. 2004, *ApJ*, 603, 139, doi: [10.1086/381241](https://doi.org/10.1086/381241)